Pseudo-One-Dimensional Magnonic Crystals for High-Frequency Nanoscale Devices

Chandrima Banerjee, Samiran Choudhury, Jaivardhan Sinha, and Anjan Barman*

Department of Condensed Matter Physics and Material Sciences,
S. N. Bose National Centre for Basic Sciences, Block JD, Sector III, Salt Lake, Kolkata 700 106, India

(Received 3 March 2017; revised manuscript received 28 June 2017; published 27 July 2017)

The synthetic magnonic crystals (i.e., periodic composites consisting of different magnetic materials) form one fascinating class of emerging research field, which aims to command the process and flow of information by means of spin waves, such as in magnonic waveguides. One of the intriguing features of magnonic crystals is the presence and tunability of band gaps in the spin-wave spectrum, where the high attenuation of the frequency bands can be utilized for frequency-dependent control on the spin waves. However, to find a feasible way of band tuning in terms of a realistic integrated device is still a challenge. Here, we introduce an array of asymmetric saw-tooth-shaped width-modulated nanoscale ferromagnetic waveguides forming a pseudo-one-dimensional magnonic crystal. The frequency dispersion of collective modes measured by the Brillouin light-scattering technique is compared with the band diagram obtained by numerically solving the eigenvalue problem derived from the linearized Landau-Lifshitz magnetic torque equation. We find that the magnonic band-gap width, position, and the slope of dispersion curves are controllable by changing the angle between the spin-wave propagation channel and the magnetic field. The calculated profiles of the dynamic magnetization reveal that the corrugation at the lateral boundary of the waveguide effectively engineers the edge modes, which forms the basis of the interactive control in magnonic circuits. The results represent a prospective direction towards managing the internal field distribution as well as the dispersion properties, which find potential applications in dynamic spin-wave filters and magnonic waveguides in the gigahertz frequency range.

DOI: 10.1103/PhysRevApplied.8.014036

I. INTRODUCTION

Periodically patterned arrays of magnetic elements in the submicron scale [1–6] have attracted wide interest over the last decade because of both the unique features of magnetism in low-dimensional systems and the potential applications in the design of magnetic storage [7], memory [8], sensors [9], and spin-based signal-processing and logic devices [10–13]. Photonic crystals, which are artificial electromagnetic dielectric materials with a periodically modulated refractive index, have already found practical applications in opto-electronics. Magnonic crystals (MCs) [11,14] can be regarded as the magnetic counterpart of photonic crystals with spin waves (SWs) acting as information carriers. In fact, since the wavelength of SWs is several orders of magnitude shorter than that of electromagnetic waves of the same frequency in photonic crystals, MCs offer better prospects for the miniaturization of microwave devices. Based on their design, MCs exhibit a characteristic Bragg scattering leading to the formation of band-gap regions of the SW spectrum in which SW propagation is prohibited [15–17]. The number and properties of the band gaps can be tuned by controlling the material and structural parameters [18,19] as well as the strength of the bias magnetic field. This tunability allows for the reliable and active manipulation of the propagation properties of SWs and makes MCs potentially useful in microwave resonators, filters, and switches operating in the gigahertz frequency range. Also, the significant reduction of SW group velocity in the vicinity of magnonic band gaps can be exploited for designing frequency-dependent delay lines. To this end, understanding the interplay between shape and intrinsic anisotropy as well as the influence of dipolar coupling in these laterally confined magnetic structures is of paramount importance for any desired application.

Hitherto, intensive research has been carried out to investigate the spin-wave dynamics in one- [16,18–21], two- [3–6,22–25], and three-dimensional [26,27] arrays of magnetic nanostructures of different shapes and compositions, which were studied using various methods ranging from analytical [such as the plane-wave method (PWM)] and computational (using micromagnetic simulations) methods to experimental means using Brillouin light scattering (BLS), ferromagnetic resonance, and time-resolved magneto-optical Kerr-effect techniques. These structures can be broadly subdivided into three groups: (i) an array of interacting ferromagnetic dots [3,5,22–24], where the dynamical coupling between the dots is due to magnetostatic interaction between the SW modes excited in the single dot. (ii) Array of periodic holes in a ferromagnetic thin film or antidot lattice [6,28,29]. Here the formation of the magnonic band structure is determined by the periodicity of the demagnetizing field around the holes in the film plane. In some cases, the holes can also be filled with another ferromagnetic material (bicomponent

*abarman@bose.res.in

MC) [25], where all the effects mentioned above are present, and the additional dipolar and exchange interactions between the two materials give additional control parameters over the magnonic band gap and propagation velocity. (iii) One-dimensional periodic waveguides in the form of microstrips, with periodically modulated compositions and structures [15,18–20,30]. All of these investigations point towards a wide range of manipulation of magnonic properties and have opened the pathway for tailoring the dispersion of high-frequency SWs in a much wider class of magnonic systems than considered so far.

Here, we introduce a pseudo-one-dimensional (1D) magnonic crystal formed by an array of asymmetric saw-tooth-shaped waveguides (ASWs) and study their magnonic band structure by experimental and theoretical methods. The topic of periodic SW waveguides studied so far includes a microscopic waveguide with periodically bent sections [31], periodic arrays of nanostrips [19], a waveguide with variable edges [16,17] or thickness [32], a ferromagnetic stripe microstructured using localized ion implantation [33], or a periodic bias magnetic field [34] and one-dimensional comblike structures [35]. In these cases, the allowed and forbidden SW modes were governed by the periodic variation of dipolar coupling, magnetization, or internal magnetic field. In our present study, the MC offers a periodic modulation of both dipolar coupling and internal magnetic field in two perpendicular directions, thereby enhancing the number of magnetic parameters to control the magnonic band structure. Here, we use the BLS technique to investigate the magnonic band structures and mode properties of the ASW arrays. We study how the magnonic band gaps can be significantly reconfigured by rotating an applied magnetic field by 20° from the SW propagation channel, i.e. the waveguide axis. In a real on-chip magnonic circuit, all the processing units are integrated along with a predefined path for data flow. Therefore, to achieve a band tunability by slightly rotating the bias field is more feasible as far as the practical implementation is concerned, as compared to rotating the entire system or changing the physical structuring. The PWM is employed to reproduce and analyze the mode characteristics. Here, the edge corrugation basically engineers the edge potential wells of the stripes, which can be used to control the mode coupling in miniature magnonic waveguides. Our findings show that this system may serve as a possible component for a tunable SW waveguide and SW signal processor, which are important components for magnonic devices.

II. EXPERIMENTAL DETAILS AND DEFINITION OF RELEVANT MAGNETIC FIELD AND WAVE-VECTOR ORIENTATIONS

A 72×72 μm^2 array of 30-nm-thick (nominal) ASWs made of polycrystalline permalloy ($Ni_{80}Fe_{20}$) is fabricated on thermally oxidized silicon substrate by means of e-beam lithography, e-beam evaporation, and lift-off process. For that, Si(001) substrate covered with 100-nm SiO_2 is spin coated with bilayer polymethyl methacrylate (495 and 950 K) positive-tone e-beam resist. On the resist-coated substrate, using high-resolution e-beam lithography, a corrugated nanostripe pattern is defined followed by development in methyl isobutyl ketone (MIBK) and isopropyl alcohol (IPA) (MIBK:IPA, 1:3) solution. Following this, on this substrate using e-beam evaporation (base pressure $= 3 \times 10^{-8}$ Torr), we deposit 30-nm-thick $Ni_{80}Fe_{20}$ at a deposition rate of 0.2 Å/S. A 2-nm-thick SiO_2 is deposited over the $Ni_{80}Fe_{20}$ using the rf sputter-deposition technique (base pressure 2×10^{-7} Torr, deposition under Ar pressure $= 5$ mTorr, deposition rate $= 0.3$ Å/S, rf power $= 60$ W). Subsequently, the lift-off is done in acetone using ultrasonic agitation to obtain the well-defined $Ni_{80}Fe_{20}$ ASW array. The scanning-electron-microscopy (SEM) image of the final structure is shown in Fig. 1(a). The length of each stripe is 72 μm (average width, 350 nm), and the nominal distance between the central axes of two consecutive stripes (a) is 800 nm. Since the edges of each stripe are patterned in an asymmetric saw-tooth-like structure, this gives rise to an additional periodicity along the stripe axes (i.e. y axis) to the otherwise 1D array of simple magnetic stripes with the periodic variation of the dipolar stray field along the z direction.

Note that due to the asymmetry in the corrugated edges, the edge-to-edge spacing between two ASWs is constant along the stripe, restricting the periodicity in the dipolar

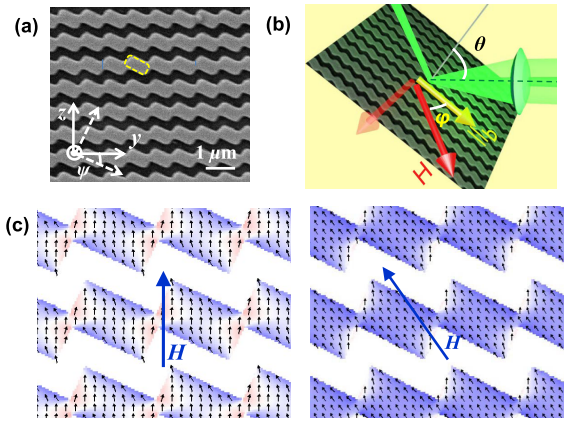

FIG. 1 (a) SEM image of the studied ASW array. The coordinate axes are shown by the white arrows. The unit cell considered for PWM calculations is marked by dashed box. (b) Schematic of the BLS measurement geometry used, showing the incident and scattered-light beams and the in-plane angle φ between the magnon wave vector q and applied magnetic field H, with both vectors lying in the sample plane. (c) Simulated static magnetic configurations (shown in red-white-blue color map) for $\varphi = 90°$ and $\varphi = 70°$ configurations (left and right panels, respectively) for $\mu_0 H = 85$ mT. The magnetic field direction is shown by blue arrows.

stray field along the y direction. In that sense, the chosen system may be termed as a pseudo-1D MC, which features two different 1D MCs in two perpendicular directions. The lattice constant (a) and Brillouin zone (BZ) edge (π/a) along the y direction are 800 nm and 3.9×10^7 rad/m, respectively.

BLS experiments are performed in the backscattering configuration for the measurement of dispersion characteristics of thermal magnons in this structure. This technique relies on an inelastic light-scattering process due to the interaction between incident photons and magnons. Monochromatic laser light (wavelength $\lambda = 532$ nm, power $= 130$ mW) from a solid-state laser is focused on the sample surface. The diameter of the laser spot is about 40 μm, hence, smaller than the array dimensions. As the laser beam is inelastically scattered from the magnons due to conservation of momentum, the magnitude of the in-plane transferred wave vector q depends on the incidence angle of light θ according to $q = (4\pi/\lambda)\ \sin\theta$. Cross-polarizations between the incident and the scattered beams are adopted in order to minimize the phonon contribution to the scattered light. Subsequently, the frequencies of the scattered light are analyzed using a Sandercock-type six-pass tandem Fabry-Perot interferometer (JRS Scientific Instruments). There, a frequency shift is observed along with the laser frequency taking into account energy and momentum conservation. The measurement geometry is shown in Fig. 1(b). Throughout the experiment, the direction of the wave vector (q) is enforced to be parallel to the stripe, i.e. the y direction, by making the stripe axes parallel to the light-scattering plane [see Fig. 1(b)], and the BLS spectra are recorded for up to two BZs, i.e. $q \sim 8 \times 10^7$ rad/m. The sample is subjected to an in-plane magnetic field of $H = 85\ \mathrm{mT}/\mu_0$ during the measurement, which can be rotated by an angle φ with the ASW axis (i.e. along q) using a precision rotary mount. In this work, we adopt two values of φ of 90° (also known as Damon-Eshbach geometry) and 70°, which correspond to two different sample magnetic configurations, as we discuss later.

III. THEORETICAL APPROACH

We calculate the spectrum of magnonic excitations of the ASW array using the PWM. This method is a popular tool because of its conceptual simplicity and its applicability to any type of lattice and any shape of scattering centers. We solve the Landau-Lifshitz (LL) equation, i.e. the equation of motion of the magnetization vector $\boldsymbol{M}(\boldsymbol{r}, t)$, under the impact of effective magnetic field $\boldsymbol{H}_{\mathrm{eff}}$, which has primarily three contributions: a uniform and constant applied magnetic field $\boldsymbol{H}$, the exchange field $\boldsymbol{H}_{\mathrm{ex}}$, and the magnetostatic field $\boldsymbol{H}_{\mathrm{MS}}$. In the linear approximation, the component $M_S(\mathbf{r})$ of the magnetization vector parallel to the static magnetic field is constant in time, and its magnitude is much greater than that of the perpendicular components $\mathbf{m}(\mathbf{r}, t)$, i.e. $|\mathbf{m}(\mathbf{r}, t)| \ll M_S(\mathbf{r})$, with $\mathbf{M}(\mathbf{r}, t) = M_S(\mathbf{r})\hat{z} + \mathbf{m}(\mathbf{r}, t)$. In a magnetically inhomogeneous medium (like a MC), the spatial inhomogeneity of the material parameters (exchange constant and spontaneous magnetization) as well as the magnetostatic field must be taken into account. Subsequently, we perform the Fourier transformation to map all the periodic functions (in space and time) including the static and dynamic parts of the magnetic fields and magnetization components to the reciprocal space using Bloch's theorem [36]. In that way, the PWM transforms the LL equation into an infinite set of algebraic equations, which leads to an eigenvalue problem. In order to find the eigenvalues (frequencies of SWs) and eigenvectors (amplitude of the dynamical component of the magnetization vector), the Fourier series has to be limited to the finite number of elements. The eigenvalue problem is then solved with standard numerical routines.

Here, we consider the lattice structure forming of permalloy and air, with two lattice vectors given by $\mathbf{a1} = a\mathbf{y}$ and $\mathbf{a2} = a\mathbf{z}$. For the calculation, we assume the magnetic field to be always oriented along the z axis, i.e. for $\varphi = 90°$ geometry along the vertical line and for $\varphi = 70°$ geometry along the line anticlockwise rotated by $\psi = 20°$. We, thus, rotate the in-plane components of the coordinate system in the clockwise direction consistent with a rotation of the magnetic field [Fig. 1(a)]. Therefore, in generalized form, the lattice vector becomes a superposition of two primitive vectors given by $\mathbf{a1} = a\cos\psi, \mathbf{y} + a\sin\psi\mathbf{z}$, and $\mathbf{a2} = -a\sin\psi, \mathbf{y} + a\cos\psi\mathbf{z}$, where $\psi = 0°$ (20°) for $\varphi = 90°$ (70°).

In the reciprocal space, the dynamic components of magnetization and magnetostatic field are expressed using Bloch's theorem, i.e. as a product of a plane-wave envelope function and a periodic function:

$$m(r) = \sum m_q(G) e^{i(q+G).r},$$

where $\mathbf{G} = (G_y, G_z)$ denotes the reciprocal lattice vector of the considered structure; in the case of the ASW array, we get $\mathbf{G} = [(2\pi)/a](n_y\cos\psi - n_z\sin\psi, n_y\sin\psi + n_z\cos\psi)$, with n_y and n_z being integers. The Bloch wave vector $\boldsymbol{q} = (q_y, q_z)$, in this case, lies along the stripe axis. So, it reads as $q = (|q|\cos\psi, |q|\sin\psi)$.

Being a periodic function of position in the MC, the saturation magnetization (M_S) and the squared exchange length ($l_{\mathrm{ex}} = \sqrt{[(2A)/\mu_0 M_S^2}$, A is an exchange constant) can be mapped onto the reciprocal space using the Fourier transformation formulas:

$$M_S(r) = \sum_G M_S(G) e^{iG.r},$$

$$l_{\mathrm{ex}}^2(r) = \sum_G l_{\mathrm{ex}}^2(G) e^{iG.r},$$

where the Fourier coefficients $M_S(G)$ and $l_{ex}^2(G)$ are determined analytically. To simplify the problem, we assume each ASW as a periodic sequence of tilted (at a 25° angle with respect to the y axis) rectangular elements (with nominal dimensions 800×400 nm^2), serially connected with each other with small overlaps [see Fig. 1(a)]. This way, the ASW array is reduced to a 2D lattice of tilted rectangles minus the overlapped region. Although the interelement exchange should be considered for more accurate calculation, the large size of the elements with respect to the exchange length of permalloy ensures that the main contribution to the collective dynamics originates from the collective dipolar field. The chosen material parameters corresponding to permalloy are saturation magnetization $M_s = 860 \times 10^3$ A/m, exchange constant $A = 1.3 \times 10^{-11}$ J/m, and $g = 2$, while small nonzero values of M_s and A are assigned to the air gap to avoid any nonphysical frequency values. A satisfactory convergence of the numerical solutions of the eigenvalue problem is obtained by taking 882 plane waves.

IV. RESULTS AND DISCUSSION

Figure 1(c) shows the static magnetic configurations of the sample with $\varphi = 90°$ and 70° (the left and right panels, respectively) simulated using OOMMF software [37] by dividing the samples into cuboidal cells of $4 \times 4 \times 30$ nm^3 volume. For $\varphi = 90°$, the static magnetic state reveals a series of 'S' states with the demagnetized regions near the edges of each stripe, as shown by the y component of magnetization encoded using a blue-white-red color map. The $\varphi = 70°$ configuration, on the other hand, shows a series of leaf states where the magnetization lies along the diagonal of each element. Here, the demagnetized regions pervade only near the smaller edge of the rectangular element and are less pronounced as compared to the $\varphi = 90°$ case. The modification in the local magnetization states changes the dipolar coupling between the elements, which eventually determines the SW character, as we show later.

For the geometry with $\varphi = 90°$, the wave-vector evolution of spin-wave frequencies, together with few representative BLS spectra (measured and calculated) are presented in Fig. 2. The calculated intensities are determined from the square of the modulus of the fundamental harmonics of magnetization in PWM, which is proportional to the signal strength detected in BLS. In Fig. 2(c), the rich magnonic band structure of the ASW array, as obtained from PWM calculations for two BZs, is shown by the blue lines, where the magnonic bands with predicted large scattering cross sections are emphasized by bold green lines. The experimental data (red solid circles) are overlaid on the calculated dispersion, which is in good agreement with the latter. In the experiment, the BLS spectra are characterized by the presence of five well-defined modes [Fig. 2(a)]. Amongst them, modes $M1$, $M2$, and $M3$ are dispersive modes, while

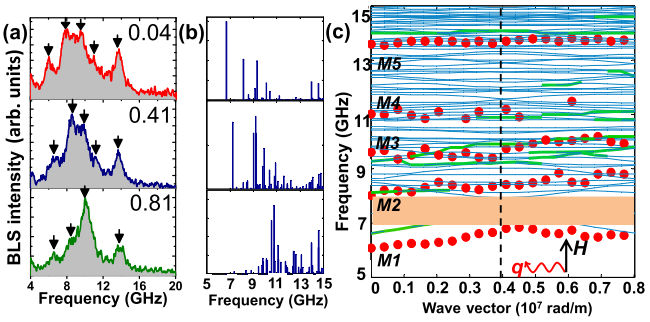

FIG. 2 (a) The Stokes side of BLS spectra taken at different values of the in-plane transferred wave vector q (denoted in units of 10^7 rad/m) for $\varphi = 90°$ geometry. The spectra are horizontally flipped for convenience. The SW peaks are indicated by the arrows. (b) Relative values of BLS intensities as calculated by PWM for different values of q given in (a). (c) Magnonic band structure in $\varphi = 90°$ geometry. Thin blue lines are PWM results. Bold green lines emphasize intense excitations as predicted by PWM. Red solid circles represent peaks in the BLS spectra. The dashed vertical line is the boundary of first BZ. The band gap is shown by the shaded region.

$M4$ and $M5$ do not significantly depend on q. In addition, at the wave vector near π/a (i.e. the edge of the first BZ), mode $M1$ undergoes Bragg diffraction, inducing the opening of a band gap of width approximately 1 GHz. The value of this gap depends upon the lattice dimensions and the cross talk between the consecutive ASWs.

In order to get closer insight into the wave-scattering mechanisms, we calculate the SW mode profiles, i.e. the modulus of the amplitude of the x component of the dynamic magnetization, of the relevant experimental modes. The spatial profiles of these modes are shown for $q = 0$, $q = \pi/a$, and $q = 2\pi/a$ (i.e. in the center and the edges of the BZs) in Figs. 3(a)–3(c), respectively. Starting from the mode profile of $M1$ at $q = 0$ [Fig. 3(a)], we find that this mode is an extended mode along the ASW axes, although with a nonuniform profile along the stripe axes. A correlation between this profile with the corresponding magnetic configuration shown in Fig. 1(c) emphasizes that this mode actually resides where the local magnetization is parallel to the external applied field, i.e. the so-called barrier or center mode of a magnetic stripe [38]. In the case of a uniform magnetic stripe, the modes are governed by the spatially inhomogeneous internal magnetic field formed by the edge potential wells due to demagnetizing effects, forming the well mode and barrier mode at the edge and central regions, respectively. As the width of the stripe is scaled down, the well mode and the barrier mode start to couple, which may create noise in the propagating signal. The corrugation at the edges lifts the demagnetized regions away from the propagation channel, thereby impeding the edge modes from occurring. In other words, the corrugation can control the extent of the edge modes, which will be useful for decoupling the center mode in

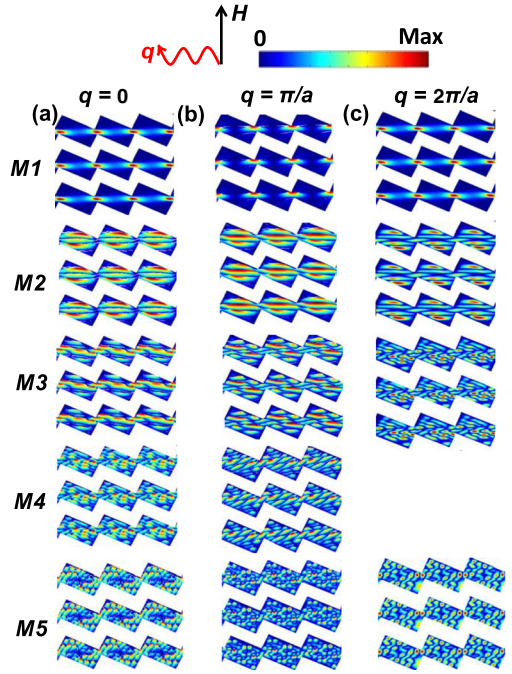

FIG. 3 Spatial profiles of the selected modes for (a) $q = 0$, (b) $q = \pi/a$, and (c) $q = 2\pi/a$ for the geometry with $\varphi = 90°$.

miniaturized magnonic devices. The spatial profiles of the higher-frequency modes $M2$ and $M3$ show that they are also quantized extended modes, with quantization number of 3 and 8, respectively, the nodal planes being perpendicular to H. The modes $M4$ and $M5$, on the other hand, show a high degree of hybridization recognized by the presence of nodal planes in both parallel and perpendicular directions to the local magnetic field. Interestingly, the mode profiles of $M4$ and $M5$ foster tunneling nodal planes through the rectangular elements, still they do not exhibit any systematic dispersion with q [see Fig. 2(c)]. The reason can be ascribed to the very high quantization number of these modes, which reduces the dynamic dipolar coupling between the rectangular elements, thereby prohibiting the mode propagation.

As we move to the mode profiles for $q = \pi/a$ [Fig. 3(b)], we observe a significant reduction in the extended character of $M1$. This is expected because at the BZ edge, as mentioned earlier, its dispersion undergoes a change from positive slope to negative slope. This substantially minimizes its group velocity $[v = d(2\pi f)/dq]$ at the BZ edge, i.e. its propagating character. The corresponding profiles for $M2$ and $M3$, on the contrary, show a more pronounced tunneling at the BZ boundary. The modes $M4$ and $M5$ continue to show an extended nature, with a slight change in their hybridization characteristics.

With further increase in q, we see substantial changes in the profiles of $M1$–$M3$. At the second BZ boundary [Fig. 3(c)], mode $M1$ regains its extended character, due to the aforementioned reason. The modes $M2$ and $M3$, on the other hand, evolve into a profile with higher quantization number. Basically, in the case of quantized modes with a high degree of quantization, the wave-vector dispersion is associated with their growth in terms of nodal planes.

In Fig. 4, the experimental and calculated frequencies are presented for $\varphi = 70°$. Note that for both values of φ, the calculated band structure exhibits mirror symmetry with respect to the boundary of the first BZ. This signifies that the wave vector is always along one symmetry direction, i.e. along the axes of ASW. As seen from Fig. 4(a), primarily four modes are observed in the BLS spectra for $\varphi = 70°$. As compared to the $\varphi = 90°$ geometry, here the frequencies of the modes are shifted to higher value, except $M4$. This trait can be attributed to the reduced demagnetized regions for $\varphi = 70°$, which enhances the internal magnetic field inside the stripe. Moreover, a suppression of spin-wave propagation is seen for $M1$; i.e. the group velocity is close to zero. Mode $M2$, on the other hand, has first an almost constant frequency up to about π/a and then it is dispersive; i.e. it has a finite slope as a function of q. This behavior leads to a marked increase in the band-gap width (approximately 1.8 GHz) as well as an upshift in its frequency position. The dispersive character of $M2$ is reproduced in the PWM results, except for the fact that the mode with highest BLS intensity [see Fig. 4(b)] is at larger frequency than $M2$. In addition, although experimentally, mode $M2$ evolves continuously with q, theoretically, the evolution of the predicted BLS intensity jumps to another frequency branch. Our findings on SW propagation and band-gap features are different from the results reported earlier for a strongly interacting magnetic stripe array, where the wave vector (of constant magnitude) was rotated in the azimuthal direction, while keeping the direction of H fixed [39].

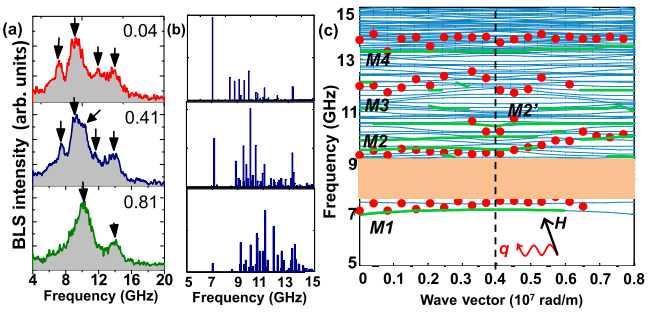

FIG. 4 (a) The Stokes side of BLS spectra taken at different values of the in-plane transferred wave vector q (denoted in units of 10^7 rad/m) for $\varphi = 70°$ geometry. The spectra are horizontally flipped for convenience. The SW peaks are indicated by the arrows. (b) Relative values of BLS intensities as calculated by PWM for different values of q given in (a). (c) Magnonic band structure in $\varphi = 70°$ geometry. Thin blue lines are PWM results. Bold green lines emphasize intense excitations as predicted by PWM. Red solid circles represent peaks in the BLS spectra. The dashed vertical line is the boundary of first BZ. The band gap is shown by the shaded region.

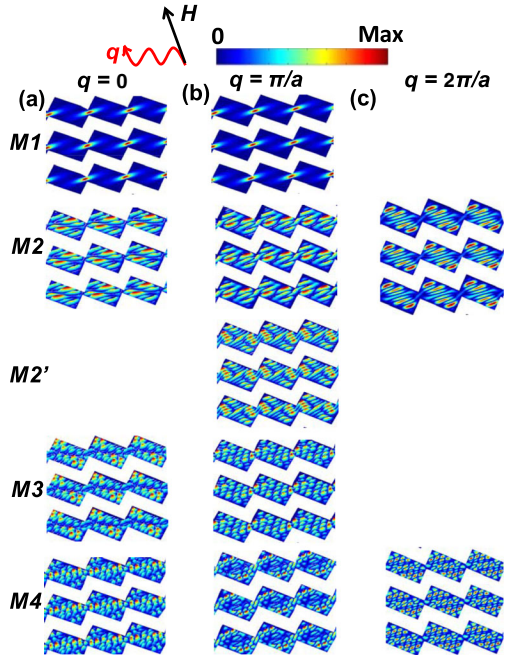

FIG. 5 Spatial profiles of the selected modes for (a) $q = 0$, (b) $q = \pi/a$, and (c) $q = 2\pi/a$ for the geometry with $\varphi = 70°$.

An inspection of the spatial spin-precession profiles of the experimentally observed modes presented in Figs. 5(a)–5(c) for $q = 0$, $q = \pi/a$, and $q = 2\pi/a$, respectively, reveals that here also mode $M1$ is a quantized mode with mode number 1, the nodal plane being perpendicular to the external field direction. Moreover, the profile of $M1$ for $\varphi = 70°$ is due to a weaker coupling of magnetic excitations between the constituent elements, thereby weakening the SW propagation [see Fig. 5(a)]. As for $M2$, it is a quantized mode with quantization number 8, similar to $M3$ in the case of $\varphi = 90°$ geometry. Nevertheless, its nodal planes are confined in the rectangular elements at $q = 0$, then it extends substantially across the interelement channels giving rise to a propagating behavior, at the edge of first BZ. At the second BZ boundary, the mode profile attains a higher quantization degree. All these trends are consistent with the dispersion behavior observed experimentally, where initially its eigenfrequency is nearly independent of q, which takes a positive slope as q approaches the BZ. The other high-frequency modes are complex hybridized modes, which show a very high quantization number and have similar properties as for the geometry of $\varphi = 90°$.

The above results demonstrate an active method of magnonic band engineering in an ASW array by merely rotating an external magnetic field with respect to the in-plane wave vector. In a practical integrated magnonic circuit, the external bias field for driving the magnons is provided either by external fields coming from a permanent magnet or by the Oersted field created by a current through a loop which also requires a cooling system. Therefore, orienting the magnetic field in a different direction is an easier way compared to increasing the field value or rotating the entire magnonic circuit. The variation in the magnetic field direction essentially leads to a modulation in the profile of a periodically varying SW channel, which subsequently determines the SW frequency dispersion. Figuratively, the SW energy incident on each rectangular element is partly reflected because the SW width profile does not fit into the narrow waveguide section at the junction of the two elements. This property can be implemented in dynamic spin-wave filters and magnonic waveguides in the gigahertz frequency range. In addition, the magnonic bands can be further tuned by changing the structural parameters of each ASW, e.g., the dimensions of the rectangular element, the interaction between the ASWs (an increase in cross talk results in reduction of band gap), the orientation and magnitude of magnetic field, and the symmetry of corrugation.

Figure 6 provides an exemplary demonstration of how the SW propagation can be manipulated in the ASW array. For that, the SW response to microwave excitation is simulated for the two φ values. Using OOMMF software, SWs are launched at the left end of the considered structure through a 400-nm-wide region. For excitation, we use a time-varying field of "sinc" profile (frequency window of 30 GHz) applied along the stripe axes. Figures 6(a) and 6(b) show the mode profiles at different SW frequencies for $\varphi = 90°$ and $\varphi = 70°$, respectively. The results reveal that the transmission of the nodal planes at 6 and 8 GHz is blocked when φ changes from 90° to 70°. On the contrary, at 9.3 GHz, the nodal planes are able to pass through for both values of φ. This asserts the possible application of the ASW array as a frequency-dependent dynamic filter. It is noteworthy that for 6 GHz in Fig. 6(a), the nonuniformity of the SW amplitude is not that pronounced as it is in the PWM results [Fig. 3(a)]. Therefore, we infer that the

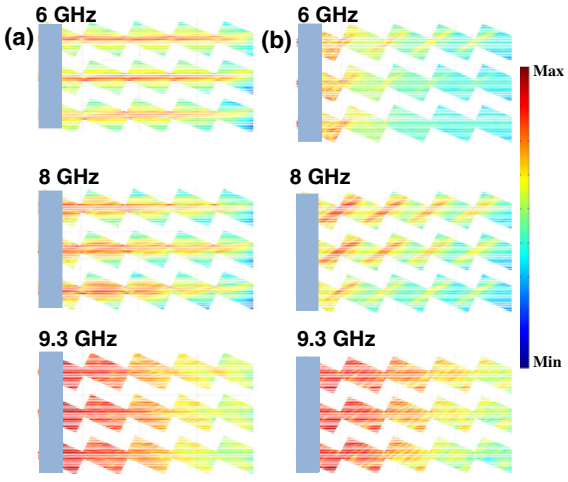

FIG. 6 Amplitude profiles of different spin-wave modes excited locally at the shaded region for (a) $\varphi = 90°$ and (b) $\varphi = 70°$ geometry.

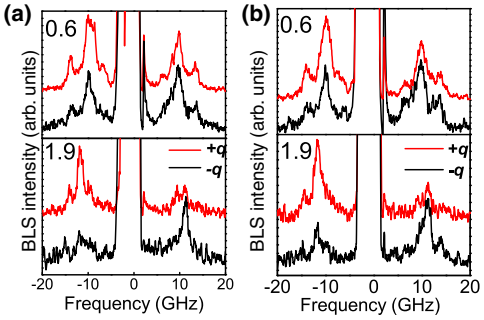

FIG. 7 BLS spectra measured at two different values of the in-plane transferred wave vector q (denoted in units of 10^7 rad/m) for (a) $\varphi = 90°$ and (b) $\varphi = 70°$ geometry. The spectra in red and black stand for two counterpropagating directions of the wave vector.

obtained nonuniformity is a result of the pinned boundary condition inherent in PWM.

Because of the lack of mirror symmetry in this system, one may expect some impression of nonreciprocal SW behavior with respect to the counterpropagating wave vectors. The nonreciprocal behavior is indeed predicted for a corrugated stripe (having mirror symmetry about its axis) with lower dimensions [40]. To verify that in our case, we measure the BLS spectra for two magnitudes of wave vectors of counterpropagating SWs. The results are presented in Figs. 7(a) and 7(b) for $\varphi = 90°$ and $\varphi = 70°$, respectively. Surprisingly, even for higher q ($=1.9 \times 10^7$ rad/m), negligible asymmetry in SW frequency values is observed for both φ values. We speculate that the reason lies in the internal field profile. When the SW propagates along either the positive or negative direction, it simultaneously perceives the profile of small and large arms of the rectangular element. Another possible reason may be the feature dimensions, which are too large for any effect of chirality to be visible. Nevertheless, a thorough investigation of the nonreciprocal behavior is of future interest.

V. CONCLUSIONS

In conclusion, we present a combined experimental and theoretical study of the reconfigurable magnonic excitations in a pseudo-one-dimensional magnonic crystal composed of ASW arrays by varying the angle (φ) between the wave vector (directed along ASW axes) and magnetic field. The switching of the magnetic field from $\varphi = 90°$ to $\varphi = 70°$ results in a transition in the internal magnetic field distribution, from the S state to the "leaf" state. Consequently, the magnonic band structure for $\varphi = 90°$ supports propagating SW modes and is characterized by a pronounced magnonic band gap. The frequency and size of the gap is effectively modified by varying φ to 70°. Further calculations of the spatial mode profiles reveal that the edge potential well modes can be effectively tuned by manipulating the edge corrugation. All these observations are important from a fundamental scientific viewpoint as well as in terms of magnonics where the tunability of spin waves is considered for magnetic nanodevices operating in the gigahertz frequency regime.

ACKNOWLEGMENTS

We acknowledge the financial support from the Department of Science and Technology, Government of India [Grant No. SR/NM/NS-09/2011(G)] and the S. N. Bose National Centre for Basic Sciences, India (Grant No. SNB/AB/12-13/96). C. B. thanks CSIR for the senior research fellowship, while S. C. thanks SNBNCBS for the senior research fellowship.

[1] A. O. Adeyeye and N. Singh, Large area patterned magnetic nanostructures, J. Phys. D **41**, 153001 (2008).
[2] J. Y. Cheng, C. A. Ross, V. Z.-H. Chan, E. L. Thomas, R. G. H. Lammertink, and G. J. Vancso, Formation of a cobalt magnetic dot array via block copolymer lithography, Adv. Mater. **13**, 1174 (2001).
[3] G. Gubbiotti, G. Carlotti, T. Okuno, T. Shinjo, F. Nizzoli, and R. Zivieri, Brillouin light scattering investigation of dynamic spin modes confined in cylindrical permalloy dots, Phys. Rev. B **68**, 184409 (2003).
[4] V. V. Kruglyak, A. Barman, R. J. Hicken, J. R. Childress, and J. A. Katine, Precessional dynamics in microarrays of nanomagnets, J. Appl. Phys. **97**, 10A706 (2005).
[5] B. Rana, D. Kumar, S. Barman, S. Pal, Y. Fukuma, Y. Otani, and A. Barman, Detection of picosecond magnetization dynamics of 50 nm magnetic dots down to the single dot regime, ACS Nano **5**, 9559 (2011).
[6] R. Mandal, S. Saha, D. Kumar, S. Barman, S. Pal, K. Das, A. K. Raychaudhuri, Y. Fukuma, Y. Otani, and A. Barman, Optically induced tunable magnetization dynamics in nanoscale Co antidot lattices, ACS Nano **6**, 3397 (2012).
[7] O. Hellwig, A. Berger, T. Thomson, E. Dobisz, Z. Z. Bandic, H. Yang, D. S. Kercher, and E. E. Fullerton, Separating dipolar broadening from the intrinsic switching field distribution in perpendicular patterned media, Appl. Phys. Lett. **90**, 162516 (2007).
[8] S. Tehrani, E. Chen, M. Durlam, M. DeHerrera, J. M. Slaughter, J. Shi, and G. Kerszykowski, High density submicron magnetoresistive random access memory (invited), J. Appl. Phys. **85**, 5822 (1999).
[9] S. H. Chung, A. Hoffmann, S. D. Bader, C. Liu, B. Kay, L. Makowski, and L. Chen, Biological sensors based on Brownian relaxation of magnetic nanoparticles, Appl. Phys. Lett. **85**, 2971 (2004).
[10] A. A. Serga, A. V. Chumak, and B. Hillebrands, YIG magnonics, J. Phys. D **43**, 264002 (2010).
[11] B. Lenk, H. Ulrichs, F. Garbs, and M. Münzenberg, The building blocks of magnonics, Phys. Rep. **507**, 107 (2011).
[12] A. Haldar and A. O. Adeyeye, Deterministic control of magnetization dynamics in reconfigurable nanomagnetic networks for logic applications, ACS Nano **10**, 1690 (2016).

[13] D. B. Carlton, N. C. Emley, E. Tuchfeld, and J. Bokor, Simulation studies of nanomagnet-based logic architecture, Nano Lett. **8**, 4173 (2008).
[14] S. A. Nikitov, P. Tailhades, and C. S. Tsai, Spin waves in periodic magnetic structures—Magnonic crystals, J. Magn. Magn. Mater. **236**, 320 (2001).
[15] Z. K. Wang, V. L. Zhang, H. S. Lim, S. C. Ng, M. H. Kuok, S. Jain, and A. O. Adeyeye, Nanostructured magnonic crystals with size-tunable bandgaps, ACS Nano **4**, 643 (2010).
[16] F. Ciubotaru, A. V. Chumak, N. Y. Grigoryeva, A. A. Serga, and B. Hillebrands, Magnonic band gap design by the edge modulation of micro-sized waveguides, J. Phys. D **45**, 255002 (2012).
[17] K. S. Lee, D. S. Han, and S. K. Kim, Physical Origin and Generic Control of Magnonic Band Gaps of Dipole-Exchange Spin Waves in Width-Modulated Nanostrip Waveguides, Phys. Rev. Lett. **102**, 127202 (2009).
[18] A. V. Chumak, A. A. Serga, B. Hillebrands, and M. P. Kostylev, Scattering of backward spin waves in a one-dimensional magnonic crystal, Appl. Phys. Lett. **93**, 022508 (2008).
[19] G. Gubbiotti, S. Tacchi, G. Carlotti, N. Singh, S. Goolaup, A. O. Adeyeye, and M. Kostylev, Collective spin modes in monodimensional magnonic crystals consisting of dipolarly coupled nanowires, Appl. Phys. Lett. **90**, 092503 (2007).
[20] M. P. Kostylev, G. Gubbiotti, J.-G. Hu, G. Carlotti, T. Ono, and R. L. Stamps, Dipole-exchange propagating spin-wave modes in metallic ferromagnetic stripes, Phys. Rev. B **76**, 054422 (2007).
[21] A. V. Chumak, P. Pirro, A. A. Serga, M. P. Kostylev, R. L. Stamps, H. Schultheiss, K. Vogt, S. J. Hermsdoerfer, B. Laegel, P. A. Beck, and B. Hillebrands, Spin-wave propagation in a microstructured magnonic crystal, Appl. Phys. Lett. **95**, 262508 (2009).
[22] V. V. Kruglyak, P. S. Keatley, A. Neudert, R. J. Hicken, J. R. Childress, and J. A. Katine, Imaging Collective Magnonic Modes in 2*d* Arrays of Magnetic Nanoelements, Phys. Rev. Lett. **104**, 027201 (2010).
[23] S. Saha, R. Mandal, S. Barman, D. Kumar, B. Rana, Y. Fukuma, S. Sugimoto, Y. Otani, and A. Barman, Tunable magnonic spectra in two-dimensional magnonic crystals with variable lattice symmetry, Adv. Funct. Mater. **23**, 2378 (2013).
[24] J. M. Shaw, T. J. Silva, M. L. Schneider, and R. D. McMichael, Spin dynamics and mode structure in nanomagnet arrays: Effects of size and thickness on linewidth and damping, Phys. Rev. B **79**, 184404 (2009).
[25] M. Krawczyk, S. Mamica, M. Mruczkiewicz, J. W. Klos, S. Tacchi, M. Madami, G. Gubbiotti, G. Duerr, and D. Grundler, Magnonic band structures in two-dimensional bi-component magnonic crystals with in-plane magnetization, J. Phys. D **46**, 495003 (2013).
[26] J. R. Vivas, S. Mamica, M. Krawczyk, and V. V. Kruglyak, Investigation of spin wave damping in three-dimensional magnonic crystals using the plane wave method, Phys. Rev. B **86**, 144417 (2012).
[27] M. Hänze, C. F. Adolff, B. Schulte, J. Möller, M. Weigand, and G. Meier, Collective modes in three-dimensional magnonic vortex crystals, Sci. Rep. **6**, 22402 (2016).
[28] M. Kostylev, G. Gubbiotti, G. Carlotti, G. Socino, S. Tacchi, C. Wang, N. Singh, A. O. Adeyeye, and R. L. Stamps, Propagating volume and localized spin wave modes on a lattice of circular magnetic antidots, J. Appl. Phys. **103**, 07C507 (2008).
[29] S. Tacchi, B. Botters, M. Madami, J. W. Kłos, M. L. Sokolovskyy, M. Krawczyk, G. Gubbiotti, G. Carlotti, A. O. Adeyeye, S. Neusser, and D. Grundler, Mode conversion from quantized to propagating spin waves in a rhombic antidot lattice supporting spin wave nanochannels, Phys. Rev. B **86**, 014417 (2012).
[30] J. Topp, J. Podbielski, D. Heitmann, and D. Grundler, Internal spin-wave confinement in magnetic nanowires due to zig-zag shaped magnetization, Phys. Rev. B **78**, 024431 (2008).
[31] V. S. Tkachenko, A. N. Kuchko, M. Dvornik, and V. V. Kruglyak, Propagation and scattering of spin waves in curved magnonic waveguides, Appl. Phys. Lett. **101**, 152402 (2012).
[32] A. V. Chumak, A. A. Serga, S. Wolff, B. Hillebrands, and M. P. Kostylev, Design and optimization of one-dimensional ferrite-film based magnonic crystals, J. Appl. Phys. **105**, 083906 (2009).
[33] B. Obry, P. Pirro, T. Bracher, A. V. Chumak, J. Osten, F. Ciubotaru, A. A. Serga, J. Fassbender, and B. Hillebrands, A micro-structured ion-implanted magnonic crystal, Appl. Phys. Lett. **102**, 202403 (2013).
[34] L. Bai, M. Kohda, and J. Nitta, Observation of spin wave modes depending on a tunable periodic magnetic field, Appl. Phys. Lett. **98**, 172508 (2011).
[35] H. Al-Wahsh, A. Akjouj, B. Djafari-Rouhani, J. O. Vasseur, and L. Dobrzynski, Large magnonic band gaps and defect modes in one-dimensional comblike structures, Phys. Rev. B **59**, 8709 (1999).
[36] M. Krawczyk and H. Puszkarski, Plane-wave theory of three-dimensional magnonic crystals, Phys. Rev. B **77**, 054437 (2008).
[37] M. J. Donahue and D. G. Porter, Interagency Report No. 6376, National Institute of Standards and Technology, 1999.
[38] V. E. Demidov, S. O. Demokritov, K. Rott, P. Krzysteczko, and G. Reiss, Nano-optics with spin waves at microwave frequencies, Appl. Phys. Lett. **92**, 232503 (2008).
[39] M. Kostylev, P. Schrader, R. L. Stamps, G. Gubbiotti, G. Carlotti, A. O. Adeyeye, S. Goolaup, and N. Singh, Partial frequency band gap in one-dimensional magnonic crystals, Appl. Phys. Lett. **92**, 132504 (2008).
[40] H.-G. Piao, J.-H. Shim, M. Yang, L. Pan, and D.-H. Kim, Selective behavior of spin wave propagation in asymmetrically modulated ferromagnetic nanowires, IEEE Trans. Magn. **51**, 11 (2015).